Effect of confinement on thick polycarbonate plates impacted by long and AP projectiles

Dorogoy A. and Rittel D. [(*)]

Faculty of Mechanical Engineering, Technion – Israel Institute of Technology, 32000, Haifa, Israel.

Abstract

The penetration process in unconfined and confined thick polycarbonate (PC) plates was investigated experimentally and numerically. The confinement was applied by insertion of the PC plate into a conical steel ring. The response of such plates to the impact of long hard steel projectiles, having an ogive-head shape in the range of velocities of 151 < V < 271 [m/s], was investigated experimentally. The results indicate that confinement results in slightly shallower depths of penetrations. Failure parameters which were determined to fit these experimental results served in simulations of these results, and also to those of a 7.62 [mm] AP projectile impacting unconfined PC targets at velocities 600 < V < 900 [m/s]. A very good agreement regarding the trajectory of the projectile was obtained. The resisting force to the penetration depends on the failure strain, whose dependence on triaxiality, temperature and strain rate, should be further investigated. The triaxiality is defined as the ratio: $t_r = \frac{\sigma_m}{\sigma_{eq}}$ where $\sigma_m = \frac{\sigma_{ii}}{3}$ and σ_{eq} is the Mises equivalent stress. The numerical results show that the confinement introduces a negative triaxiality within the confined plates prior to impact. The shallower penetration in confined targets is due to the higher negative triaxiality which reduces the ductile damage during penetration, while the hydrostatic pressure reduces the brittle fracture mechanism.

Keywords: a. polycarbonate. b. confinement. c. finite elements. d. impact e. projectiles. f. penetration.

*Corresponding author .Tel: +972-4-829-2236.

 E-mail address: dorogoy@technion.ac.il

1. Introduction

The application of confining forces to strengthen a structure is an ancient technique which induces a self-equilibrated state of stress known as prestressing. This technique has long been applied for both small and large-scale objects, including most construction materials [1]. Examples of external prestressing for the purpose of structural strengthening with steel and fiber reinforced polymers, as well as plate bonding, can be found in [2].

The working range of materials that have a low tensile strength in comparison with their compressive strength (e.g. concrete and ceramics), can be greatly increased by imposing a compressive confinement. For concrete [3], the confinement enhances significantly both the compressive strength and ultimate strain. Reinforced concrete columns by means of fiber-reinforced polymer or steel jackets are a commonly used technique [4].

Confinement of ceramic materials has been reported to improve their ballistic performance [5, 6]. The confinement was found to decrease the exit velocity in complete penetration cases, and decrease the depth of partial penetration.

Experimental studies on the effect of confinement on transparent glassy polymeric materials used as transparent armor, are quite scarce. The effect of biaxial compressive prestress of a PMMA (aka plexiglass) plate was investigated by [7]. The shrink fit insertion technique was used to apply equi-biaxial confinement without impairing target transparency. The authors performed preliminary ballistic impacts at speeds of ~130 m/s and reported a significant reduction of radial cracking due to the prestress. A hybrid *experimental-numerical* investigation was recently conducted in [8] on the effect of *high prestress* on the ballistic performance of thick PMMA monolithic plates. The plates were subjected to ballistic impacts of long ogive-headed projectiles launched at velocities in the range of 165 – 260 [m/s]. A conical insertion technique was used to apply high levels of prestress. The observations of this work showed beyond any doubt that confinement markedly increases the ballistic resistance of PMMA by significantly reducing both the ductile and brittle damage mechanisms.

Polycarbonate (PC) is rated as highly resistant to impact and perforation, and is therefore used as lightweight transparent armor (protection) in a wide range of applications. The characterization of its static and dynamic flow, and failure properties has been carried out by numerous investigators [9, 10-14, 15]. An experimental–numerical investigation of the penetration and

perforation of a thick polycarbonate (PC) plates by a short armor piercing 7.62 [mm] projectile was reported in [16]. In that investigation, the trajectories, penetration velocities, depths of penetration, and the damage zone around the trajectories of the projectile were fully characterized. It was concluded that the projectile's trajectory in the PC is mainly due to ductile damage, while the tensile pressure adds up and influences the direction and, to a lesser extent the depth of penetration.

Deep penetration and perforation tests of PC plates having various thicknesses, by ogive-nosed projectiles were recently conducted [17,18]. The projectiles impacted normally at velocities in the range of 500-900 [m/sec]. The results of these tests show that a nearly constant value of the specific cavitation energy can be identified, which is practically independent of both the impact velocity and aspect ratio of the target. Consequently, the available body of experimental data covers now a wide range of impact velocities and projectiles' shapes, including confined targets at the lower velocities. It is therefore of interest to model all the available experimental data in a unified way, such as to identify consistent trends of the ballistic response of polycarbonate over a wide range of impact velocities.

Therefore, this paper addresses the effect of confinement on ballistic performance of thick PC plates subjected to ballistic impacts of long ogive-headed projectiles traveling at velocities in the range of 150 – 300 [m/s]. It also predicts the performance of thick PC monolithic plates subjected to normal ballistic impacts of 7.62 [mm] armor piercing (AP) projectiles traveling at velocities in the range of 600 – 900 [m/s], based on the experimental results reported in [17]. The conical insertion technique developed in [8] is used here again, to apply high levels of prestress. The experiments are supplemented with 3D transient non-linear adiabatic finite element simulations using the commercial finite element code Abaqus 6.12-2 [19]. The numerical results are validated by a comparison of the predicted maximum depths of penetration (DOP) to actual experimental DOP's, velocities and resisting force during the ballistic penetration process.

The paper is organized as follows: Following the introduction, comes a description of the experimental impact results. The test setup and assembly which have been used in previous investigations ([8], [20]) are detailed in appendix A.

A numerical section comes next. A preliminary static axisymmetric simulation of the confining process comes first followed by a 3D dynamic simulation of confinement and penetration. The 3D geometry, mesh, analysis type as well as the material models, failure criteria and properties

which have been used in previous investigations ([8], [16], [20]), are all detailed in appendix B. Then, a proper mesh size is chosen with the aid of mesh convergence tests. A study of the effect of the failure strains on the penetration results ensues. The numerical penetration results come next, and are presented in two separate subsections: 1) Long projectiles at low impact velocities, 2) AP projectiles at high impact velocities. The numerical results at low impact velocities for confined and unconfined targets are compared to the experimental results obtained in this investigation. The numerical results of high impact velocities of unconfined targets are compared to the results of [17], and a prediction of the effect of confinement for high velocity impact is presented. The experimental and numerical sections are followed by discussion and conclusions sections.

2. Experimental results

Thick polycarbonate (PC) plates were impacted by long hard steel projectiles. The projectiles were accelerated by a gas gun. The procedure is fully detailed in [8, 20]. The projectiles are stabilized in their flight by means of a polymeric sabot which gets destroyed upon impact. Two types of target plates were impacted: confined and unconfined. The projectile, sabot and targets as well as the assembly are all detailed in Appendix A.

Eight impact tests were performed on 3 unconfined targets (I,II,III) and nine impacts on 3 confined targets (IV,V,VI). Each target was impacted 2-4 times. The tests are summarized in Table 1 in which the measured impact velocities and their corresponding DOP's are detailed. The impact velocities were in the range $151 < V < 271$ [m/s].

The targets were sectioned and polished to visualize the trajectories and DOP's. The accuracy of the measured DOP's is estimated to be ± 1 [mm]. The DOP's of the confined targets are slightly smaller than those in the unconfined targets (see Fig. 8 in the sequel). Pictures of the trajectories within an unconfined target are shown in Fig. 1a-b, and in Fig. 1c-d for a confined target, respectively. Three distinct damage zones can be observed: cavity, cracked zone and plastically deformed zone. These regions were also observed in [16 - 17]. The cavity has a variable residual diameter, which is consistently smaller than that of the projectile's core, as an indication of

4

significant post-perforation recovery of the material. The cavities are narrower at the end of the trajectory because of the ogive-head shape. The cracked zones in the confined and unconfined targets differ significantly. The cracks in the unconfined target are fine and narrow, while those in the confined targets are thicker.

3 Numerical simulations

The purpose of the numerical simulations is to provide insight into the penetration process, and serve as a predictive tool for future ballistic tests. The geometries, meshes, types of analyses, material models and properties, failure criteria and parameters are all detailed in appendix B. These parameters have been thoroughly described in [8], [16] and [20]. A static axisymmetric simulation of the insertion process which is used to apply confining pressures is done first, using Abaqus standard finite element code [19]. 3D dynamic impact simulations of the penetration process in confined and unconfined targets are performed using *Abaqus explicit* [19]. For the penetration simulations, a numerical convergence test for a mesh size is done first. A constant mesh size, which yields numerical results close to the experimental results, is chosen. The chosen mesh size remains then fixed for all the subsequent simulations.

The effect of the failure strains on the penetration into confined and unconfined targets is then studied followed by simulation results of the tests.

 Results of two types of penetration simulations are described:

   1) Penetration of long projectiles at velocities in the range of $120 - 340$ [m/s] (table 1).

   2) Penetration of AP projectiles at velocities in the range of $600 - 900$ [m/s] ([17]).

The simulations show the projectile's depths of penetration, velocities and accelerations during the penetration process for both confined and unconfined targets.

3. 1 Static confinement results

A preliminary static axisymmetric numerical analysis was performed to determine the resulting pressures, triaxialities and plastic strain (if any) within the inserted plates. The geometry, mesh and material data are detailed in appendix B.1 and B.4.3. The variations of the pressure, Mises stress and plastic strains within the confined plates upon completion of the

insertion step are all detailed in Fig. 2. The pressure is shown in Fig. 2a. The pressure at the center of the target lies in the range 45 - 57 [MPa]. The Mises equivalent stress distribution is shown in 2b and lies in the range $67 - 78$ [MPa] at the center of the target. Hence, *the triaxiality is ~ - 0.7* at the center of the target prior to impact. The triaxiality is defined as the ratio: $t_r = \frac{\sigma_m}{\sigma_{eq}}$ where $\sigma_m = \frac{\sigma_{ii}}{3}$ and σ_{eq} is the Mises equivalent stress. Due to the high level of confinement, some plastic deformation develops inside the target. The plastic equivalent strain variations (PEEQ) are shown in Fig. 2c. The center of the plate experiences *very small* plastic strains of less than 1%.

3.2 Mesh convergence check

It was shown in [16] that the numerically calculated DOP of a 0.3" AP projectile into a PC plate is mesh dependent. Hence this investigation starts with a mesh dependency check. The problem of a normal impact at 160 [m/s] of an unconfined target was solved using 7 seed sizes of mesh in the region shown in Fig. B2b. The region adjacent to the projectile trajectory was meshed with hexahedral equal size mesh using seed = 0.5, 0.75, 1.0, 1.25, 1.5 1.75 and 2.0 [mm]. The corresponding depths of penetration (d) versus time (t) are shown in Fig. 3a, and the corresponding velocities (V) versus time are shown in Fig. 3b.

It can be observed that the results are *indeed mesh dependent*. The finer the mesh size, the deeper the penetration, corresponding to a lower the resisting force. The results for a wide range of mesh size 1.25 [mm] < seed < 1.75 [mm] are surprisingly close to each other considering the velocities and the *maximum depth of penetration* (DOP). The numerical results are not just close to each other but also close to the observed experimental results. The experimental results for the DOPs due to normal impact at 161 and 166 [m/s] are listed in table 1 and are 17 and 18 [mm] respectively. Fig. 4 shows the effect of the mesh size on the DOPs. It can be observed that the gradient becomes moderate for mesh size greater than 1 [mm]. Since a mesh size of 2 [mm] is too coarse, it is concluded that a suitable mesh size is within the region 1.25 [mm] < seed < 1.75 [mm] ,where the DOPs differ by only 2.2 [mm] which corresponds to 13% of the experimental

value of 17 [mm] for V = 161 [m/s]. Hence a constant mesh size of 1.25 [mm] was chosen for all the subsequent analyses. This mesh size was also found to yield converged results to the experimental results in [16].

3.3 Effect of the failure strain

Fracture of metals is sensitive to the triaxiality of the stress. This has long been shown in the classical experimental work of Bridgman [20]. The analytical work [21] laid the basis for the effect of void growth. An exponential relation between the fracture strain versus (compression) triaxiality was observed in [22]. Such an exponential relation was also observed lately in [23],[24]. The effect of triaxiality, strain rate and temperature on the failure strains of PC needs to be thoroughly investigated. When we tried to simulate the penetration into PC without assuming a rise in the failure strain due to compression triaxiality, the obtained results were too deep. Hence we deliberately introduced a linear rise in the failure strain due to triaxiality. By using a trial and error process we could fit the experimental results of Table 1 by using the failure stains, as shown in Fig. 5. This is the only difference in the properties of the PC which are listed in appendix B and those used in [16]. Here the failure strains at negative triaxiality for all strain rates grow linearly with an angle $\theta = 124^o$, as shown in Fig. 5. Such an angle was found by a trial and error procedure, to best reproduce the experimental results (DOP) obtained for the low velocity impact tests, as shown in the sequel..

The effect of the failure strain increase at negative triaxiality on the depths of penetration was investigated for an impact velocity of 160 [m/s], using the assembly shown in appendix A. Three types of failure strains were investigated. The three types differed by the angle θ which is shown in Fig. 5: $\theta = 180^o$, 143° and 124°. The value of $\theta = 180^o$ was used in [16]. For this case, the failure strain depends only on the strain rate. The depths of penetration for confined and unconfined targets are shown in Fig. 6. It can be observed that the higher the failure strain, the lower the depth of penetration. It can also be observed that the analyses predict a slightly deeper penetration in unconfined targets in comparison with confined ones. The bounce back effect, which is evident also in PMMA [8,20], exists for all the three investigated angles. Table 2

summarizes the DOPs and the time to complete halt for the three types of failure strains. It is evident that the DOPs of confined targets are smaller than those of unconfined, irrespective of the selected value of the failure strain which were tested.

The numerical DOPs obtained with $\theta = 124^o$ are 18 and 17 [mm] for unconfined and confined targets, respectively, while the experimental results of table 1 are 17 and 14 [mm] correspondingly. Since the numerical results correspond well with the experimental ones, the failure strains of $\theta = 124^o$ were adopted in all the subsequent analyses.

3.4 *Low velocity impact of confined and unconfined targets by long rod ogive-nose projectiles*

The numerical results of confined and unconfined targets (appendix A) impacted at various impact velocities are reported now. Seven impact velocities were tested numerically: 120, 160, 200, 240, 280, 320, and 360 [m/s]. The unconfined target was fully perforated at 320 [m/s], although the projectile was stopped. The confined target was fully perforated at impact velocities $V_i > 340$ [m/s] . A comparison between confined and unconfined targets for the variation of the DOP at impact velocities 160, 240 and 320 [m/s] is shown in Fig. 7. It can be observed that the projectiles penetrate slightly deeper in unconfined targets. It means that the confinement is adding resistance to penetration. It can also be observed that after reaching the *maximum depth of penetration* (DOP) the projectiles bounce backwards. The unconfined target impacted at 320 [m/s] is exceptional because the projectile perforates the plate, but get stuck within it.

The DOPs for all the tested impact velocities, as well as the experimental results are shown in Fig.8. The numerical results are fitted using a polynomial of the type: $DOP(V) = aV + bV^2$. The coefficients for the confined and unconfined DOPs are determined as $a = 0.074870,\ b = 0.0001454$; $a = 0.07381,\ b = 0.0002033$, respectively. The numerical results of the unconfined targets agree very well with the experimental results. The numerical results of the confined targets agree fairly well with the experimental results, and predict slightly

deeper DOPs (1-2 [mm]). For the given element size of 1.25 [mm], this result can be considered as a good agreement.

A comparison of the penetration velocity for confined and unconfined targets due to impact velocities oft 160, 240 and 320 [m/s] is shown in Fig. 9. It can be observed that the deceleration in the confined targets is slightly higher since the projectiles lose their velocity quicker. Three regions can be distinguished: I) Entrance. II) Penetration. III) Bounce back. These regions are marked in Fig. 9 for impact velocity of 160 [m/s].

The first region lasts for 40 – 50 [μs] in which the velocity change is small . The second region lasts until the projectile reaches its DOP. The third region corresponds to backward bouncing of the projectile with a positive velocity.

To get the decelerations the penetration velocities were derived using central finite difference with Δt=15 [μs] and then smoothed using Savitzki-Golay algorithm with 9 points. The deceleration for impact velocities 160, 240 and 320 [m/s] for confined and unconfined targets are shown in Fig. 10. It can be observed that the decelerations for impact velocities 240 and 320 [m/s] increase until they reach a flat maximal level. This level is the same for all impact velocities above 200 [m/s]. For an impact velocity of 160 [m/s], the projectile stops before reaching the maximum deceleration. The maximal flat value of the confined target is slightly higher than for the unconfined targets and is marked by the dashed lines in Fig. 10. The difference is approximately Δa=100,000 [m/s^2]. The deceleration for 7 impact velocities vs. the penetration velocity in the confined targets is plotted in Fig. 11. This figure clearly shows the maximum flat level to which the decelerations reach for impact velocities 240, 280, 320 and 360 [m/s]. It can also be observed that deceleration due to lower impact velocities 200, 160 and 120 [m/s] does not reach the maximum flat value. It can also be observed that the decelerations drop to zero when the velocity direction changes and becomes positive.

The maximal flat level of the deceleration, when multiplied by the mass of the projectile, represents the maximum resisting force that the PC exerts on the projectile. The fact that the deceleration for *impact velocity higher than 240 [m/s]* reaches a flat region indicates that the

DOP in thick plates subjected to high velocity impact can be estimated using a simple formula

such as $DOP \approx \dfrac{1}{2}\dfrac{V_i^2}{a}$, where a is the deceleration in the flat area.

3.5 High impact velocity of an AP projectile

3.5.1 Deep penetration

The deep penetration into 100x100xT [mm] polycarbonate plate with thicknesses, T, ranging from 300 to 500 mm at impact velocities (V_i) $600[m/s]<V_i<900[m/s]$ was investigated experimentally [17]. Ogive-tip armor-piercing (AP) projectiles (type M61) with a diameter of 7.62 [mm], total mass of 9.91 [gr] and shank length 32.4 [mm] were accelerated by a powder gun. The trajectories of the projectiles were monitored using a high speed camera. The penetration trajectories for seven normal impact tests are detailed.

These trajectories were simulated numerically in this work. A PC cylinder, with diameters of 100 [mm] and length of 360 [mm] was used as target in the analysis. Because of symmetry of the problem, only one quarter of the model is simulated. The same mesh size along the trajectory was used, ie 1.25 [mm]. The model and mesh is shown in appendix B5.

The numerical DOP results as well as the experimental results of [17] are detailed in table 3. The difference between the experimental and numerical DOP results is also detailed in table 3. The difference [%] between the DOPs is calculated by $\dfrac{DOP^{(i)}_{numerical} - DOP^{(i)}_{experimental}}{DOP^{(i)}_{experimental}} \times 100$. The percent difference between the time to full halt (ΔT) is calculated similarly. A very good agreement can be noted between the numerical simulations and the experimental results, given the difference is less than $|7[\%]|$ for the whole range of impact velocities.

The experimental trajectories of [17] and the computed trajectories due to 6 additional impact velocities: 624, 701, 735, 773, 857 and 905 [m/s], are all plotted in Fig. 12. Fig. 12a shows the

depth of penetration vs time ((d [mm]) vs. t [ms]), while Fig. 12b shows the same results but normalized. The normalization which is: $\dfrac{d^{(i)}}{DOP^{(i)}}$ vs. $\dfrac{t^{(i)}}{\Delta T^{(i)}}$, where i corresponds to the impact velocity and is detailed in the column 1 of table 3.

An excellent agreement can be observed in Fig. 12a between the experimental and numerical results. The curves in Fig. 12b converge to a universal curve which can be put in the form [17]:

$$\frac{d}{DOP} = \xi_1\left(\frac{t}{\Delta T}\right) - \frac{1}{2}\xi_2\left(\frac{t}{\Delta T}\right)^2 + \frac{1}{3}\xi_3\left(\frac{t}{\Delta T}\right)^3 \quad \text{where} \quad (\xi_1,\xi_2,\xi_3) = (2.133,\ 2.463,\ 0.2626) \quad \text{are}$$

coefficients.

3. 5.2 Effect of confinement

  A normal impact of the AP projectile (M61) traveling at 750 [m/s] on the PC target of Fig. A2 was simulated numerically. Two cases were solved: 1. Unconfined. 2. Confined. In both cases the projectile perforated the target. The velocity variation during the perforation is shown in Fig. 13. The predicted exit velocity for the unconfined target is 618 [m/s] and for the confined target 586 [m/s]. The confinement seems to cause the target to have higher resisting force, which slows down the projectile's exit velocity by $\Delta V = 32[m/s]$ compared to the unconfined target.

It must be noted that the results *depend highly on the input failure properties, especially the plastic failure strain of the PC vs strain rate and triaxiality*. The values used (Fig. 5) were calibrated to fit the experimental results at the low velocities. A proper investigation, which will identify the failure strain of PC vs strain rate, temperature and triaxiality, is still needed.

While the effect of the confinement on the ductile failure (DOP, penetration velocities) at high impact velocities requires experimental assessment - the effect of the confinement on the brittle failure has already been shown for PMMA [8]. It is quite obvious that the confinement will prevent cracking and the transparency of the PC targets will be retained after multiple hits.

Discussion

The ballistic performance of thick confined and unconfined PC plates was investigated experimentally and numerically. The behavior of the plates subjected to low velocity impact $150 < V_0 < 300$ [m/s], of long steel ogive-headed projectiles have been investigated experimentally. The experimental results were complemented by numerical analyses which added insight into the effects of ductile failure strains and pre-impact confinement. The numerical analyses were also applied to high impact velocities by short AP projectiles (L/D < 5, L – length of projectile, D – diameter of projectile) of unconfined PC targets. The results were compared to the experimental results of [17]. A prediction of the effect of confinement for high velocity impact is also added. The numerical results show good agreement with the experimental ones regarding the confined and unconfined targets at low impact velocities by long projectiles. They are also in excellent agreement with the experimental trajectories [17] within an unconfined target impacted by "short" AP projectile at a higher velocity region $600 < V_0 < 900$ [m/s].

The results indicate that three phases can be identified in the projectile trajectory: I) Entrance. II) Penetration. III) Bounce back. These phases are similar to those observed in [25]. These regions are related to the resisting force that the target exerts on the projectile. During the entrance phase the resisting force grows with the penetration depth and reaches a maximum value. This resisting force is only slightly reduced during the penetration process, but can nevertheless be assumed to be approximately constant. This fact is with agreement of the results of [17]. During the bounce back phase, the resisting force drops to zero.

If the targets are impacted at low velocity impact (less than 200 [m/s]), the resisting force does not reach its maximum value. The first phase is the largest, while for high impact velocity (higher than 200 [m/s]), the second phase is the dominant (lasts longer and responsible for most of the depth of penetration). The velocity drop for high velocities during the entrance phase is quite similar and can be estimated from Fig. 11 to be 70 – 100 [m/s]. The increasing deceleration during the entrance phase may be interpreted in terms that during perforation of thin targets, the resisting force is variable and does not reach its maximum value. The perforation of thin targets is done while the projectile does not reach its maximum resisting force and the perforation might be considered as done in the "entrance phase" of our results.

Two failure mechanisms work jointly during penetration of polymers: ductile and brittle failure. The penetration in PC is mostly due to ductile failure since PC is not brittle. Its static mode I fracture toughness at room temperature is ~ 4 times of that of PMMA, but multiple shots might nevertheless cause fracture. The effect of the confining pressure on the brittle failure is quite obvious [8] - It will prevent cracking and retain the transparency of the PC targets even for multiple hits. Our experimental results for long projectiles and low velocities (Table 1 and Fig. [8]) indicate that the confinement slightly reduces the DOPs'. This means that the confinement introduces a resisting force which is higher than that of unconfined targets. We could fit these results numerically by introducing failure strains which are triaxiality-dependent as shown in Fig. 5. Using these failure strains we could get excellent agreement with the trajectories of a 7.62 [mm] AP projectile impacting at high velocity range 600 – 900 [m/s]. Adding confinement numerically while keeping the same failure strains, which were correlated with the low velocity impacts, reveals that the confinement will reduce the penetration speeds, hence resulting in shallower DOP's, including impact by high velocity short projectiles. These results *depend highly on the input failure properties. A thorough investigation which will identify the failure strain of PC vs strain rate, temperature and triaxiality is still needed.*

The numerical results are mesh-dependent. A question arises: "what is the suitable mesh size?" The mesh size, which yields a proper resisting force to penetration which must be found in penetration tests is the suitable. Tests should be done at high enough impact velocities in order to get the flat region of the deceleration. If the tests provide the whole trajectory than the second derivative with time provides the deceleration. If only the DOP is known from a test than the deceleration can be estimated by using the relation $a = \dfrac{V_i^2}{2 \cdot DOP}$ where V_i is the impact velocity.

The resisting stress for a projectile can than be estimated by $\sigma_r = \dfrac{F_r}{A} = \dfrac{a\,M}{A}$ where a is the value of the "flat deceleration", M is the mass of the projectile and A is the cross sectional area of the projectile. The resisting force depends on the shape of the head of the projectile. For example in [25] it was found that ogive head projectiles are the most efficient penetrators as they cause the lowest resisting force to penetration. It was found in [25] that the resisting force of a blunt head projectile is slightly higher (~10%) than that of the hemispherical-head projectile, and much

higher (~200%) than that of ogive-headed projectiles. A coefficient may be fitted to each head shape and only a few tests might be enough for correlation of numerical analyses.

Conclusions

- Three phases can be identified in the projectile trajectory: I) Entrance. II) Penetration. III) Bounce back (if incomplete penetration).

- There is an upper limit for the resisting force that a PC target can exert on a projectile.

- The upper limit is reached during the second phase "penetration" and remains almost constant during that phase.

- For high velocity impacts, the penetration phase is long in comparison to the first and third phases hence the resisting force may be considered as constant.

- In lower velocity impacts (less than 200 [m/s]) the second phase is not reached, hence the resisting forces (decelerations) are variable during the whole penetration process.

- The confinement of a PC target seem to prevent brittle fracture (shattering) due to impacts.

- The confinement of a PC target seem to increase the resisting force to penetration, which is exerted on a projectile. This has been observed at low impact velocities, and should be verified experimentally at high impact velocities.

- Numerical results are mesh dependent and should be calibrated with experimental results to yield the appropriate resisting force during penetration.

- The numerical results depend highly on the input of the failure properties hence a thorough investigation which will identify the failure strain of PC vs strain rate, temperature and triaxiality is needed.

References

[1] Gasparini D. The prestressing of structures: A historical review. Proceeding of the second international congress on Construction History, Queen's College, Cambridge University , 2006; 2: 1220-32

[2] Nordin H. Strengthening structures with externally prestressed tendons. Literature review, Luleå University of Technology Technical Report 2005-06.

[3] Lam L, Teng JG. Design-oriented stress-strain model for FRP-confined concrete; Source: CONSTR BUILD MATER 2003; 17(6-7): 471-89

[4] Rocca, Silvia , Galati, Nestore, Nanni, Antonio. Review of design guidelines for FRP confinement of reinforced concrete columns of noncircular cross sections Source: J COMPOS CONSTR 2008; 12(1): 80-92.

[5] Anderson CE, Royal-Timmons SA. Ballistic performance of confined 99.5%-Al_2O_3 ceramic tiles. INT J IMPACT ENG 1997; 19: 703:13.

[6] Holmquist TJ, Johnson GR. Modeling projectile impact onto prestressed ceramic targets. J PHYS IV 2003; 110: 597:602.

[7] Archer JS, Lesser AJ. Impact resistant polymeric glasses using compressive pre-stress. J APPL POLYM SCI 2009; 114: 3704–3715.

[8] Dorogoy A. , Rittel D. Impact of thick PMMA plates by long projectiles at low velocities. Part II: Effect of confinement. MECH MATER 2014; 70:p 53-66.

[9] Ravi-Chandar K. On the failure mode transitions in polycarbonate under dynamic mixed-mode loading. INT J SOLIDS STRUCT 1995;32:925-38.

[10] Rittel D, Levin R, Maigre H. On dynamic crack initiation in polycarbonate under mixed-mode loading. MECH RES COMMUN 1997;24(1):57-64.

[11] Rittel D, Levin R. Mode-mixity and dynamic failure mode transitions in polycarbonate. MECH MATER 1998;30(3):197-216.

[12] Rittel D. On the conversion of plastic work to heat during high strain rate deformation of glassy polymers. MECH MATER 1999;31(2):131-9.

[13] Rittel D. Experimental investigation of transient thermoplastic effects in dynamic fracture. INT J SOLIDS STRUCT 2000;37(21):2901-13.

[14] Moisa S, Landsberg G, Rittel D, Halary JL. Hysteretic thermal behavior of amorphous semi-aromatic polyamides. POLYM J 2005; 46(25):11870-5.

[15] Sarva S, Mulliken AD, Boyce MC. Mechanics of Taylor impact testing of polycarbonate. INT J SOLIDS STRUCT 2007;44:2381-400.

[16] Dorogoy A, Rittel D, Brill A. Experimentation and modeling of inclined ballistic impact in thick polycarbonate plates. INT J IMPACT ENG 2011; 38(10): 804–14.

[17] Weiss A, Vizel A, Durban D. An experimental investigation of deep penetration into polycarbonate targets. 27th international symposium on ballistics 2013; Freiburg, Germany, April 22-26.

[18] Weiss A, Durban D. Experimental Assessment of the Specific Cavitation Energy in Polycarbonate Plate Perforation. Proceedings of the 54th IACAS, February 19-20, 2014. Haifa, Israel.

[19] Abaqus/CAE version 6.12-2. Providence, RI, USA: Dassault Systemes Simulia Corp.

[20] Bridgman PW. Studies in Large Plastic Flow 1952 ;McGraw-Hill.

[21] Rice JR, Tracey DM. On the ductile enlargement of voids in triaxial stress fields. J MECH PHYS SOLIDS 1969 ;17:201–217.

[22] Johnson G, Cook W. Fracture characteristics of three metals subjected to various strains, strain rates and temperatures. ENG FRACT MECH 1985;21:31–48.

[23] Dorogoy A, Rittel D. Numerical validation of the shear compression specimen. Part I: quasi-static large strain testing. EXP MECH 2005; 45(2):167–177.

[24] Karp B, Dorogoy A, Rittel D. A Shear Compression Disk Specimen with Controlled Stress Triaxiality Under Dynamic Loading . EXP MECH 2013; 53:243–253.

[25] Rittel D, Dorogoy A. Impact of thick PMMA plates by long projectiles at low velocities. Part I: Effect of head's shape. MECH MATER 2014; 70: 41–52.

[26] Anderson CE. An overview of the theory of hydrocodes. INT J IMPACT ENG 1987;5:423-39.

[27] Abaqus/CAE version 6.12-2. Abaqus documentation Abaqus analysis user's manual. Dassault systemes. New York: Springer; 2009 chapters 20-21.

[28] Hazell PJ, Roberson CJ, Moutinho M. The design of mosaic armour: the influence of tile size on ballistic performance. MATER DES 2008;29:1497-503.

[29] Bauwens-Crowet C, Bauwens JC, Homes G. The temperature dependence of yield of polycarbonate in uniaxial compression and tensile tests. J MATER SCI 1972;7:176-83.

[30] Rittel D, Dorogoy A. A methodology to assess the rate and pressure sensitivity of polymers over a wide range of strain rates. J MECH PHYS SOLIDS 2008;56:3191-205.

TABLES and FIGURES

Table 1: Experimental details.

Specimen	type	Number of shots	Velocity [m/s]	Depth of penetration [mm]	Test number
I	unconfined	1	not measured	-	1
I	unconfined	2	161	17	15
II	unconfined	1	202	25	2
II	unconfined	2	172	20	3
II	unconfined	3	166	18	4
III	unconfined	1	not measured	-	5
III	unconfined	2	173	19	13
III	unconfined	3	151	16	14
IV	confined	1	156	14	6
IV	confined	2	161	14	7
IV	confined	3	161	14	8
V	confined	1	166	15	9
V	confined	2	167	13	10
V	confined	3	151	13	11
V	confined	4	not measured		12
VI	confined	1	271	26	16
VI	confined	2	271	28	17

Table 2:
The DOPs and time to complete halt due to three types of failure strains: $\theta = 180^{\circ}$, 143° and 124° (Fig. 5) for confined and unconfined targets.

	$\theta = 124^{\circ}$		$\theta = 143^{\circ}$		$\theta = 180^{\circ}$	
	T [ms]	DOP [mm]	T [ms]	DOP [mm]	T [ms]	DOP [mm]
unconfined	0.189	18.0	0.258	23.2	0.337	29.7
confined	0.177	17.0	0.213	19.3	0.295	27.2

Table 3:
Experimental [17] and numerical DOP and time to complete halt (ΔT) for M61 AP
projectile impacting PC plate.

i	Velocity [m/s]	Experimental [17]		Numerical		Relative difference	
		DOP [mm]	ΔT [ms]	DOP [mm]	ΔT [ms]	DOP [%]	ΔT [%]
1	624	141	0.467	146	0.483	3.2	3.3
2	701	183	0.541	179	0.521	-2.1	-3.8
3	735	200	0.553	199	0.582	-0.3	5.3
4	773	228	0.603	220	0.601	4.6	-0.3
5	857	282	0.671	263	0.657	-6.8	-2.1
6	905	302	0.679	287	0.690	-4.9	1.7

Dorogoy A. and Rittel D.

thin cracks

18 [mm]

Plastic region

a.

b.

thick cracks

14 [mm]

Plastic region

STAINLESS

c.

d.
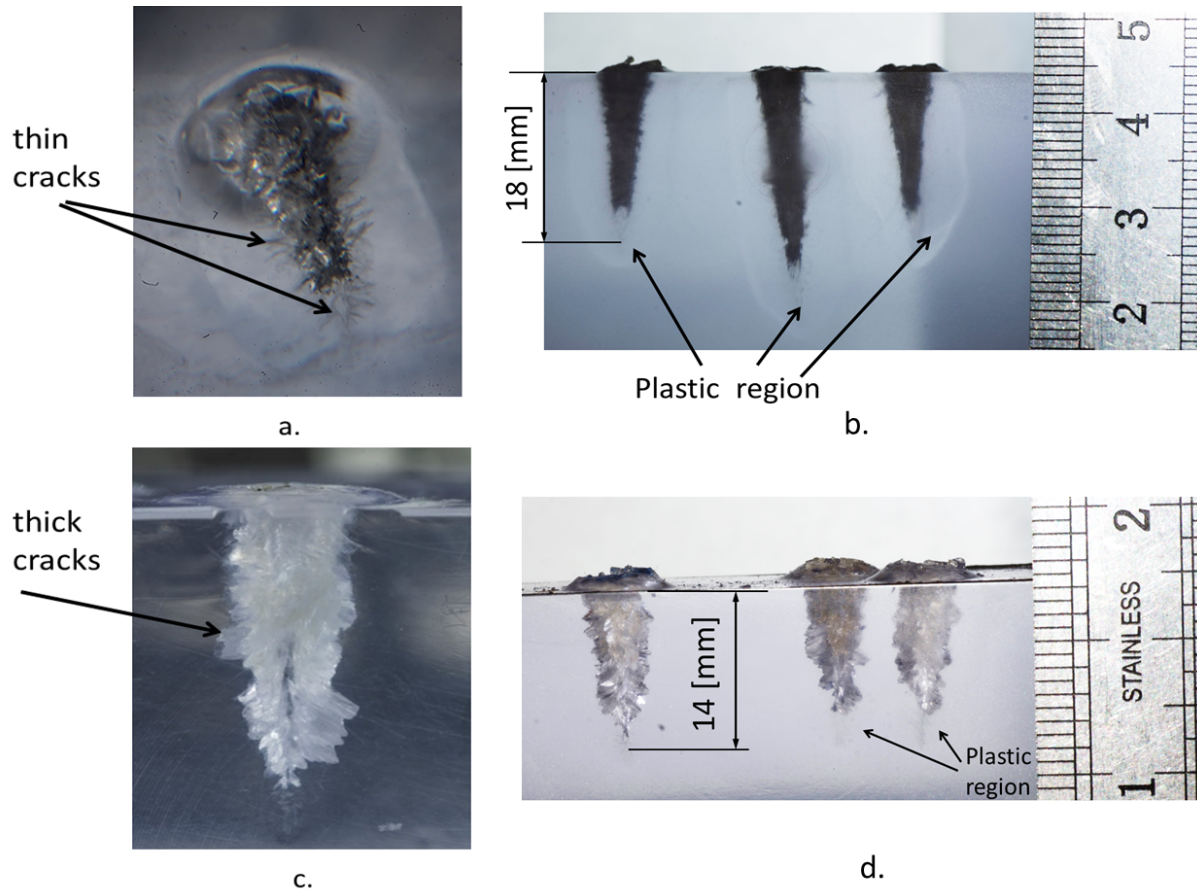
Figure 1: a and b: A typical trajectory within unconfined target. c and d: Trajectories within a confined target.

Dorogoy A. and Rittel D.

S, Pressure [Pa]

+9.090e+07
+7.953e+07
+6.817e+07
+5.681e+07
+4.545e+07
+3.409e+07
+2.272e+07
+1.136e+07
+0.000e+00
-9.870e+07

a.

S, Mises [Pa]

	+4.602e+08
	+8.957e+07
	+7.838e+07
	+6.718e+07
	+5.598e+07
	+4.479e+07
	+3.359e+07
	+2.239e+07
	+1.120e+07
	+0.000e+00

b.

PEEQ

	+3.880e-02
	+3.395e-02
	+2.910e-02
	+2.425e-02
	+1.940e-02
	+1.455e-02
	+9.700e-03
	+4.850e-03
	+0.000e+00
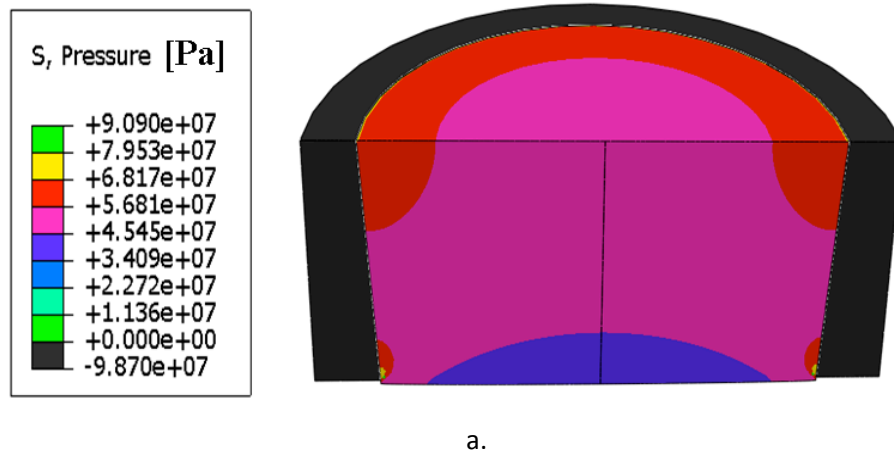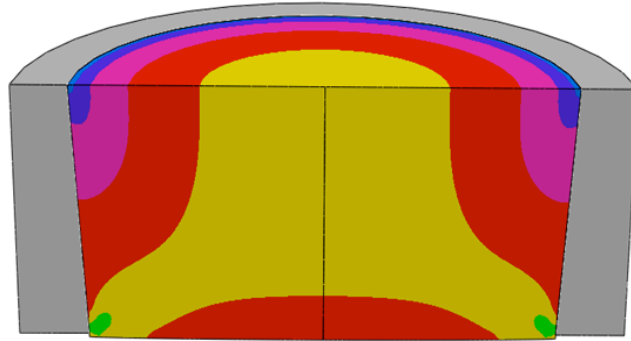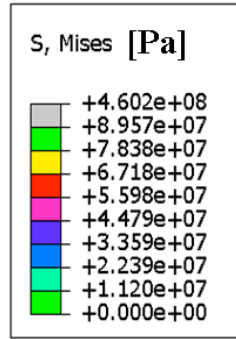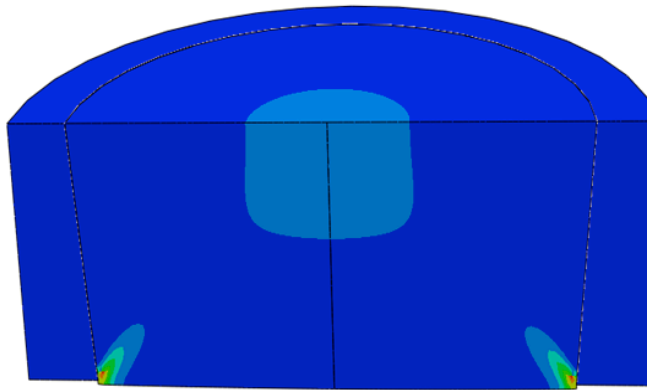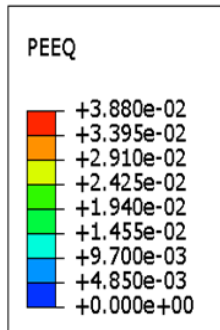
c.

Figure 2: Distributions of pressures (a), Mises stress (b), and equivalent plastic strains (PEEQ) within the targets at the end of the insertion process (c).

Dorogoy A. and Rittel D.
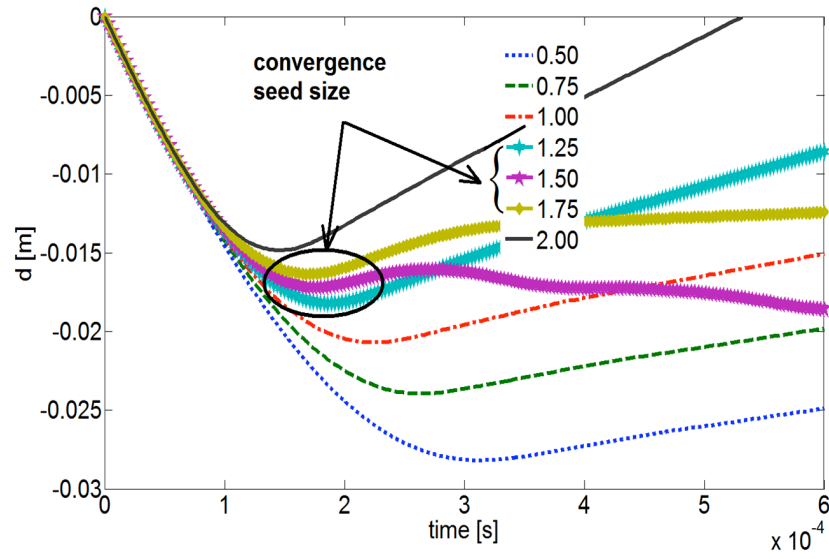
a.
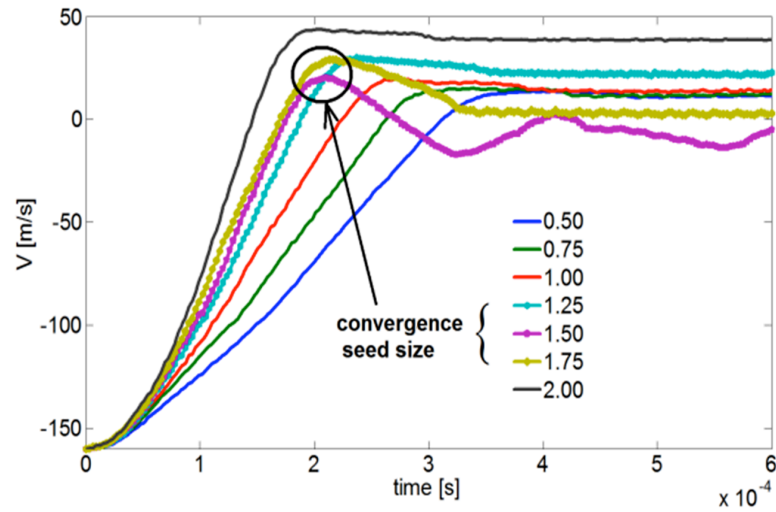
b.

Figure 3: Numerical mesh convergence tests for seed = 0.5, 0.75, 1.0, 1.25, 1.5 1.75 and 2.0 [mm]. a. Depth of penetration. b. Velocities of penetrations.

Dorogoy A. and Rittel D.
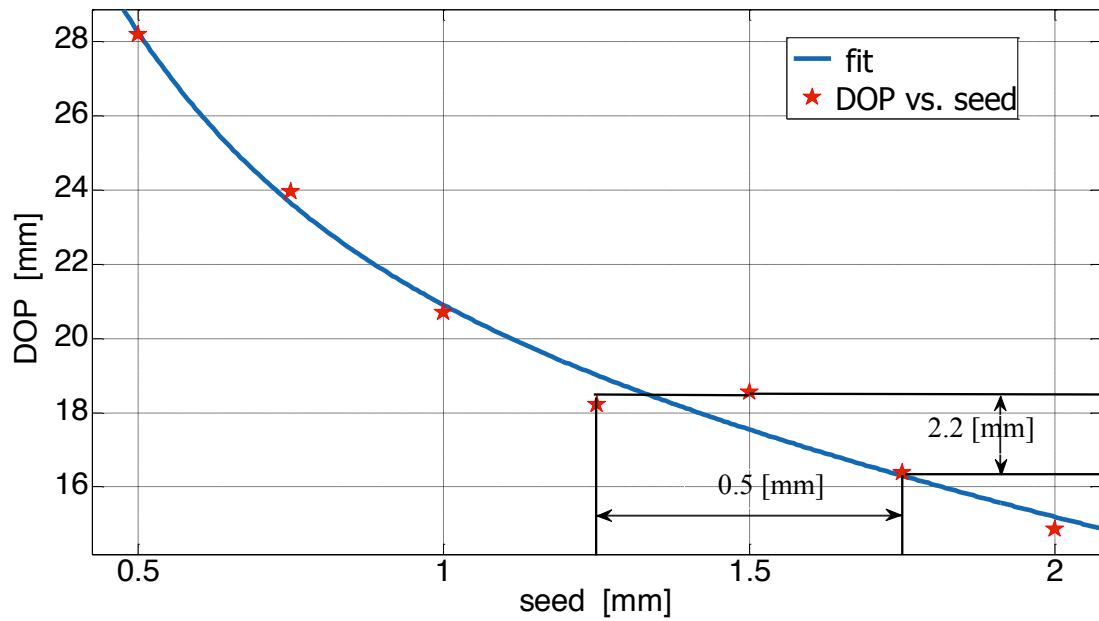
Figure 4: The DOPs versus the mesh size for seed = 0.5, 0.75, 1.0, 1.25, 1.5 1.75 and 2.0 [mm].

Dorogoy A. and Rittel D.
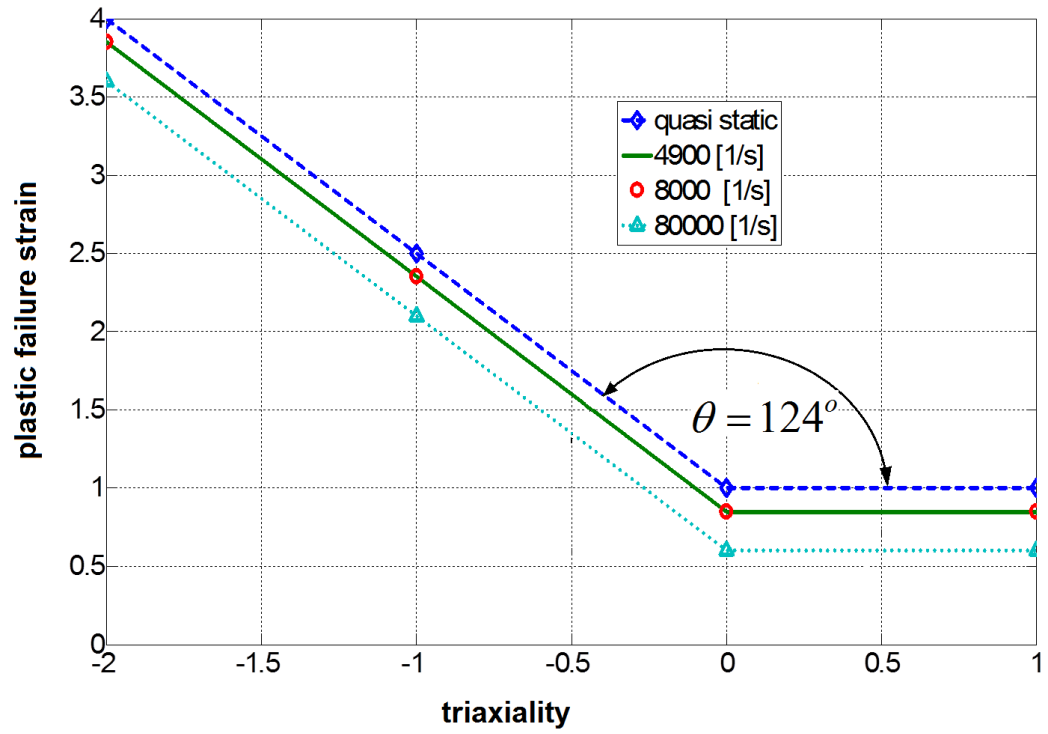
Figure 5: Equivalent plastic failure strains vs triaxiality for various strain rates.

Dorogoy A. and Rittel D.
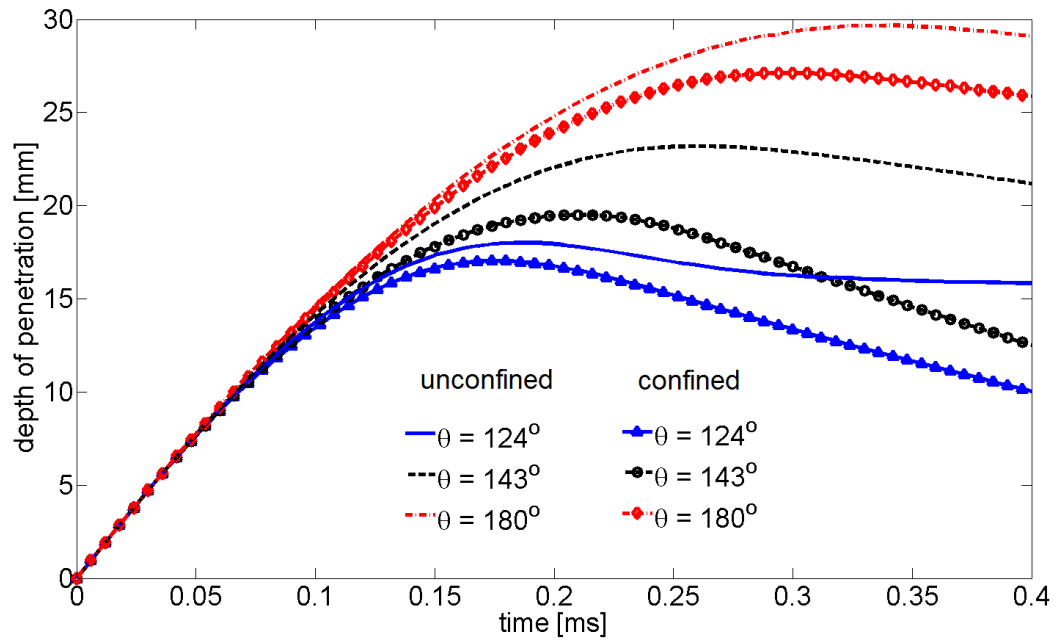
Figure 6: The depths of penetration versus time due to impact velocity of 160 [m/s]. Two types of targets: confined and unconfined. Three types of failure strains: $\theta = 180^o$, 143° and 124°.

Dorogoy A. and Rittel D.
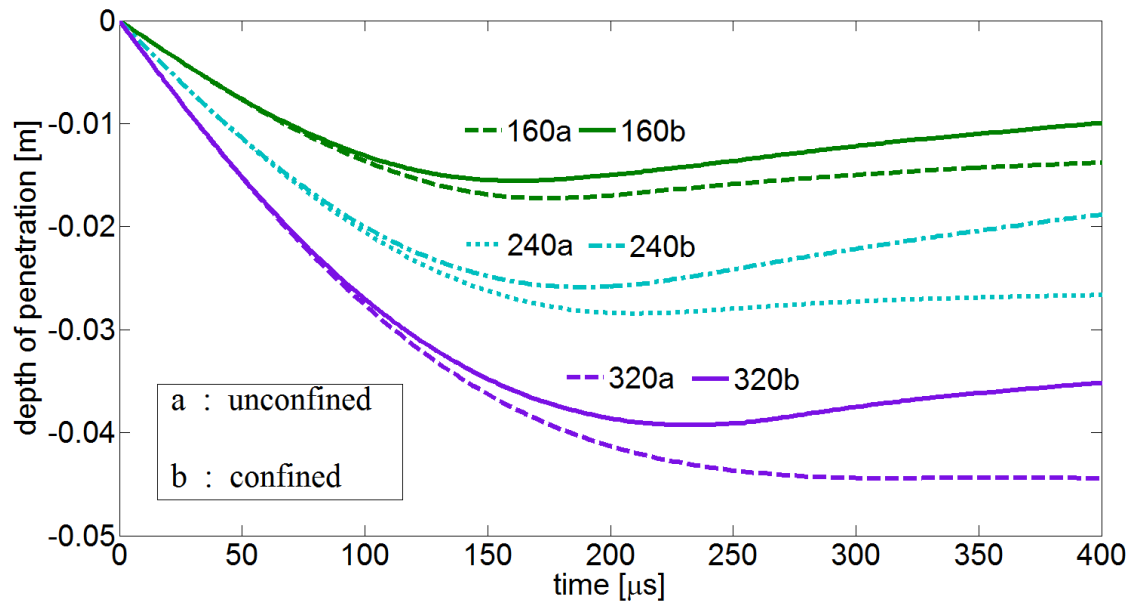
Figure 7: The depth of penetration due to impact velocities: 160, 240 and 320 [m/s] for confined and unconfined targets.
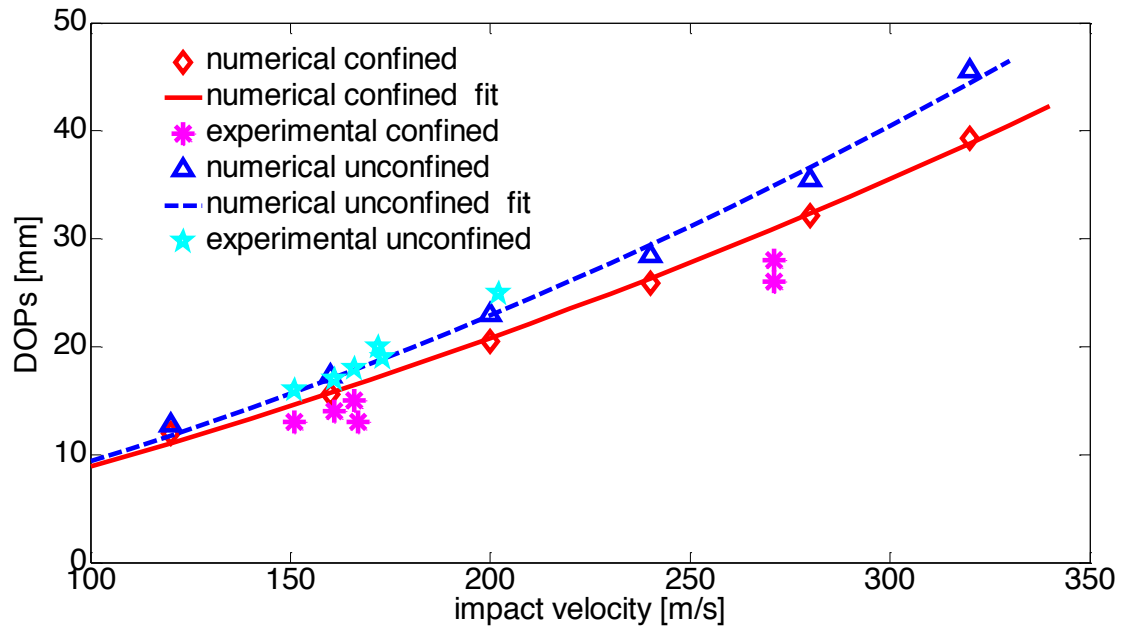
Figure 8: A comparison of the numerical DOPs due to impact velocities: 120, 160, 200, 240, 280 and 320 [m/s] for confined and unconfined targets, along with experimental results.
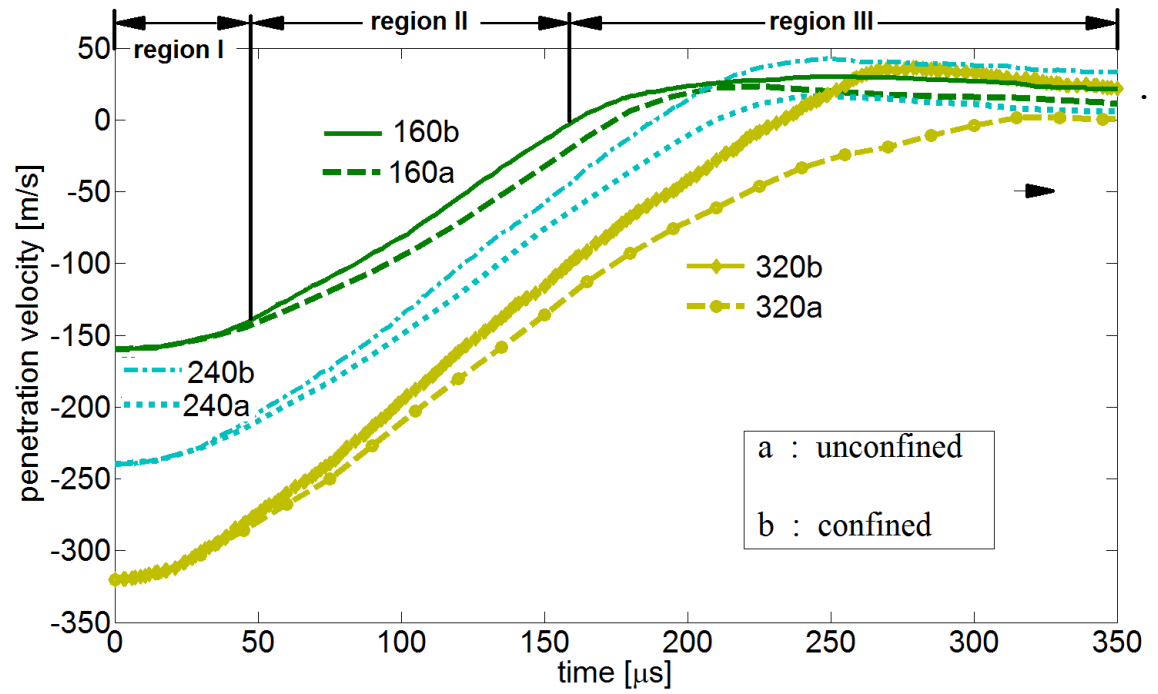
Figure 9: A comparison of the penetration velocities due to impact velocities: 160, 240and 320 [m/s] for confined and unconfined targets.

Dorogoy A. and Rittel D.
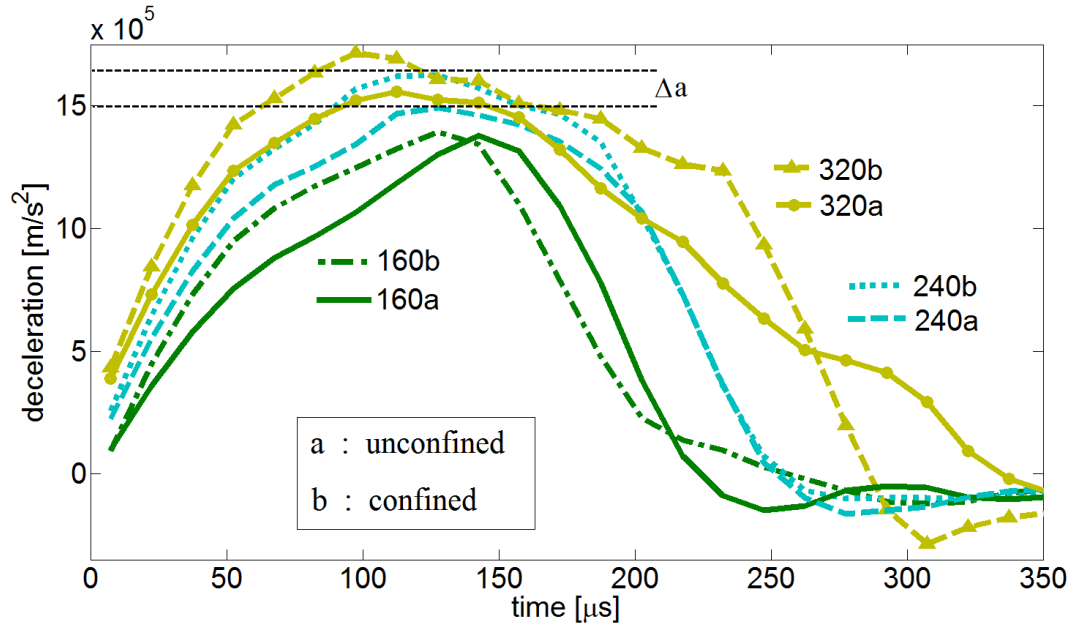
Figure 10: The deceleration for impact velocities 160, 240 and 320 [m/s] for confined and unconfined targets.
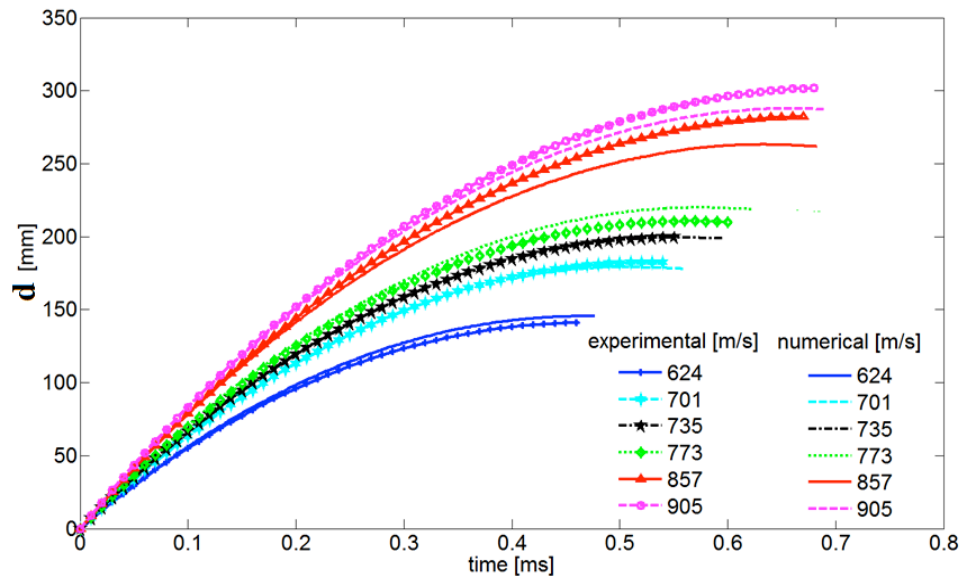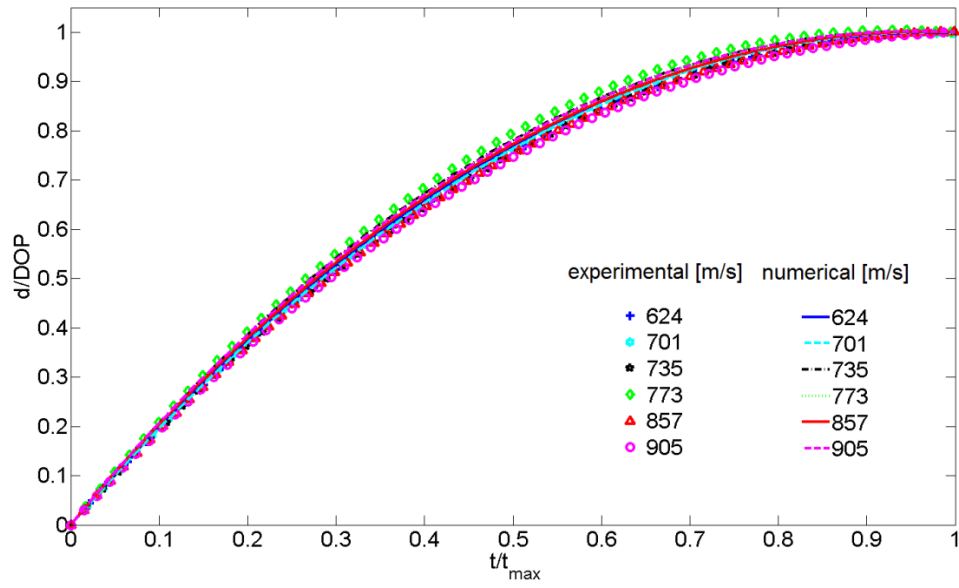
Dorogoy A. and Rittel D.
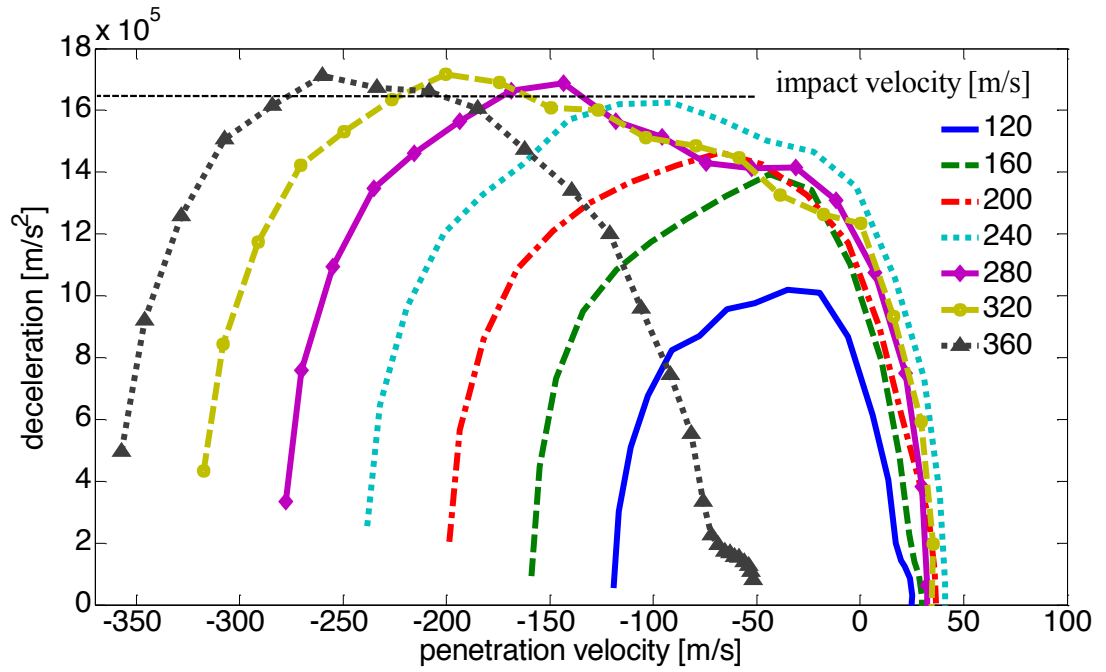
Figure 11: Deceleration vs penetration velocities for confined target impacted 120, 160, 200, 240, 280, 320 and 360 [m/s].

Dorogoy A. and Rittel D.

a.

b.

Figure 12: The experimental [17] and numerical trajectories. a. Physical units. b. Normalized.
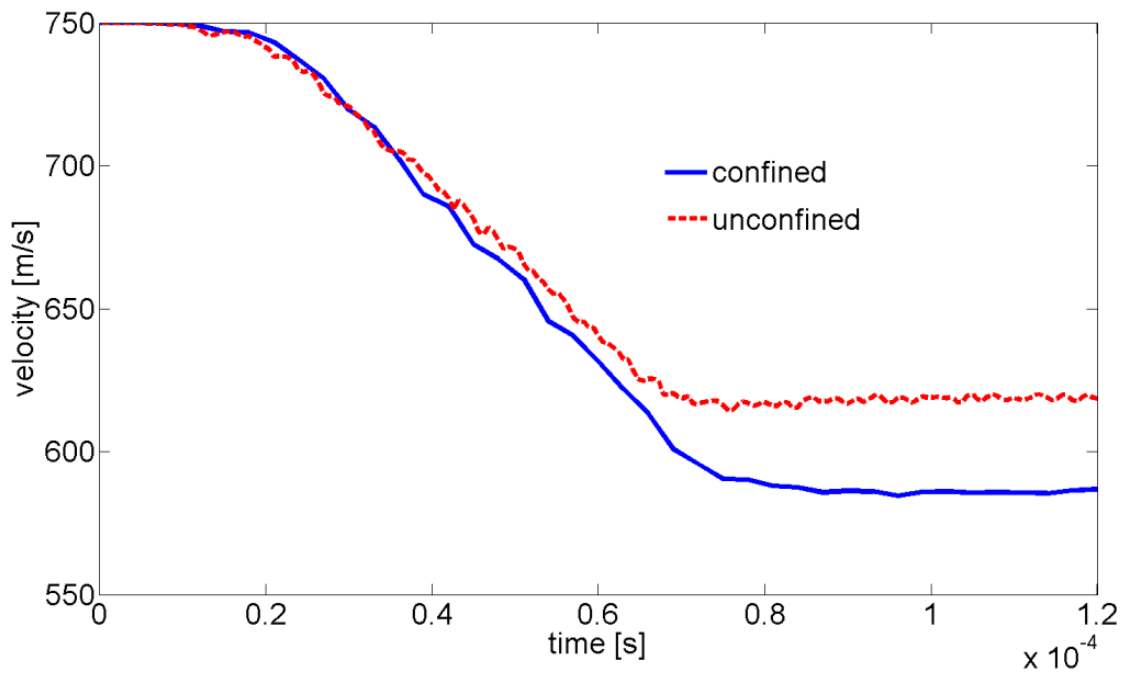
Dorogoy A. and Rittel D.

Figure 13: Velocity variation during perforation of an AP projectile (M61) of confined and unconfined target.

APPENDIX A

A.1 Projectile and sabot

The projectile which is shown in Fig. A1a was made of hard stainless steel and weighed 11.4 [gr]. It had a diameter D = 6 [mm] and length L = 56 [mm]. Its head was ogive-shaped corresponding to 3CRH (Caliber Radius Head, [8, 20]).
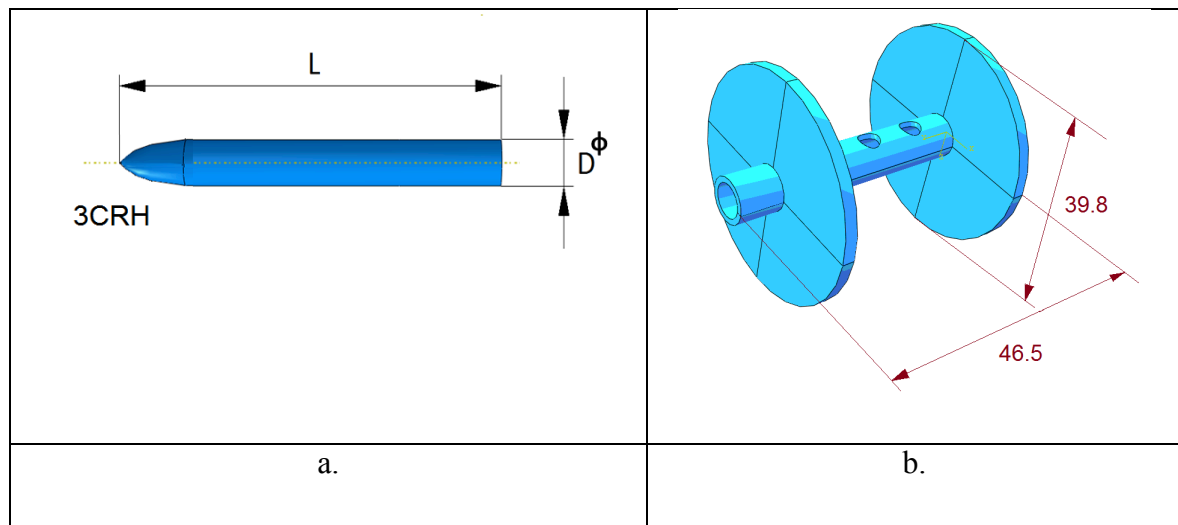

| a. | b. |

Figure A1 : a. The steel projectile having an ogive head corresponding to 3CRH. b. The polymeric sabot.

The sabot is made by Objet 3D printer from FullCure720 which is a rigid, general purpose semi translucent acrylic-based photopolymer. The sabot is shown in Fig. A1b with its overall dimensions. Its weight is 6.5 [gr].

A.2 Confined and unconfined targets

The confined plates were round with conical 86° side faces, as shown in Fig. A2a. The plates were inserted into a confining hard steel sleeve (Fig. A2b) with an inner conic face of 86°.   The misfit between the outer radius of the plate and the inner radius of the confining ring was 1 [mm]. The dimensions of the confining ring are shown in Fig. A2. The thickness of both the plates and the confining ring was 40 [mm]. The plates are considered "thick" since t/D = 6.67 where D is the projectile diameter ("thin" plates would

correspond to t/D<1).   The plates were inserted into the confining ring using an MTS servo-hydraulic machine.   The faces in contact were lubricated prior to insertion using silicone oil and water-displacing spray (WD40).
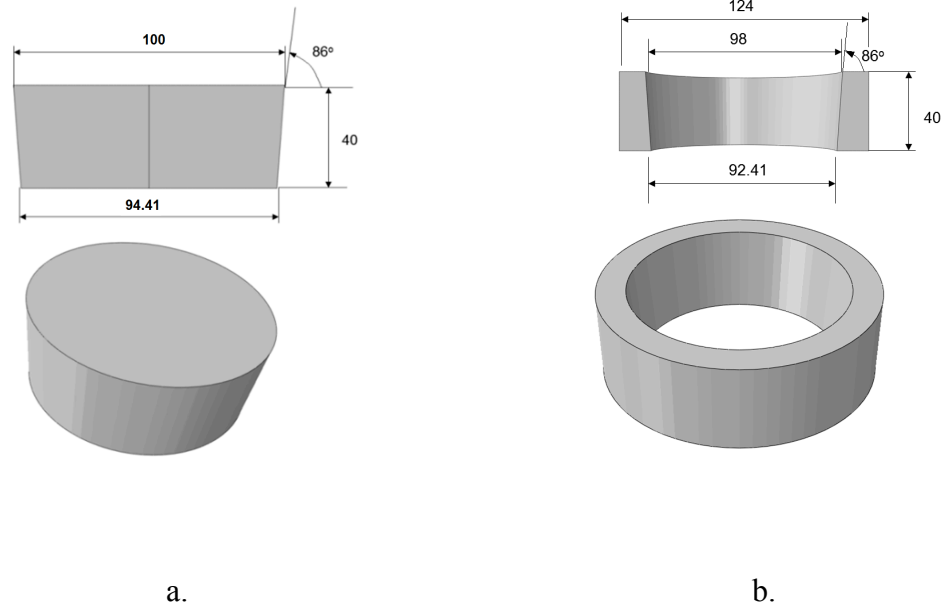

a.   b.

Figure A2: a. The round PC plate. b. The confining steel ring.

APPENDIX B

B. 1 Axisymmetric analysis of confinement

The axisymmetric model which consists of the PC plate and confining steel ring is shown in Fig. B1. Vertical displacements were applied on the upper face of the plate. Symmetry conditions were applied on the bottom face of the confining ring. Symmetry was also applied at r = 0 (axisymmetric analysis). The properties are detailed in appendix B. Since the insertion process is done while the materials are below their elastic limit - the PC was modeled as an elastic-plastic material model with Mises plasticity while the steel was modeled as an elastic material. The properties are detailed in appendix B.4. The meshed axisymmetric model, shown in Fig. B1, consists of 1960 linear quadrilateral elements of type CAX4R on the PMMA plate. 520 linear quadrilateral elements of type CAX4R were used for the ring. The typical element size was ~1 [mm].
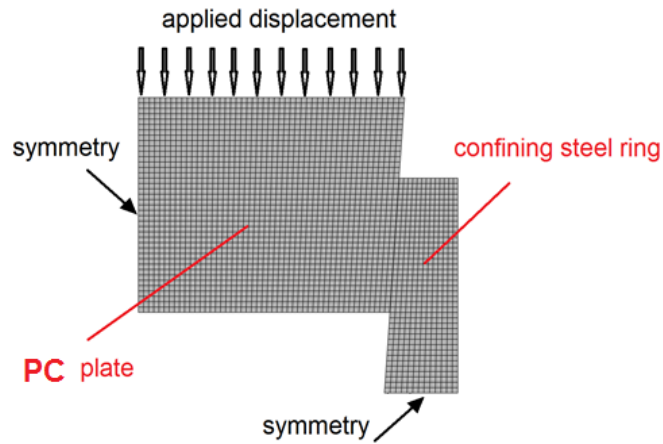
Figure B1: The meshed axisymmetric model

B.2. Geometry and mesh

The geometry model of the confined target consist of the confining steel ring, the PC plate, the steel ogive head projectile and the polymeric sabot. The geometry of the unconfined target is similar but does not contain the steel confining ring. Because of symmetry only half of the physical parts were modeled. Symmetry conditions were applied along the cut. Fig.   B2a shows the assembly of the parts of the confined target at the beginning of analysis.
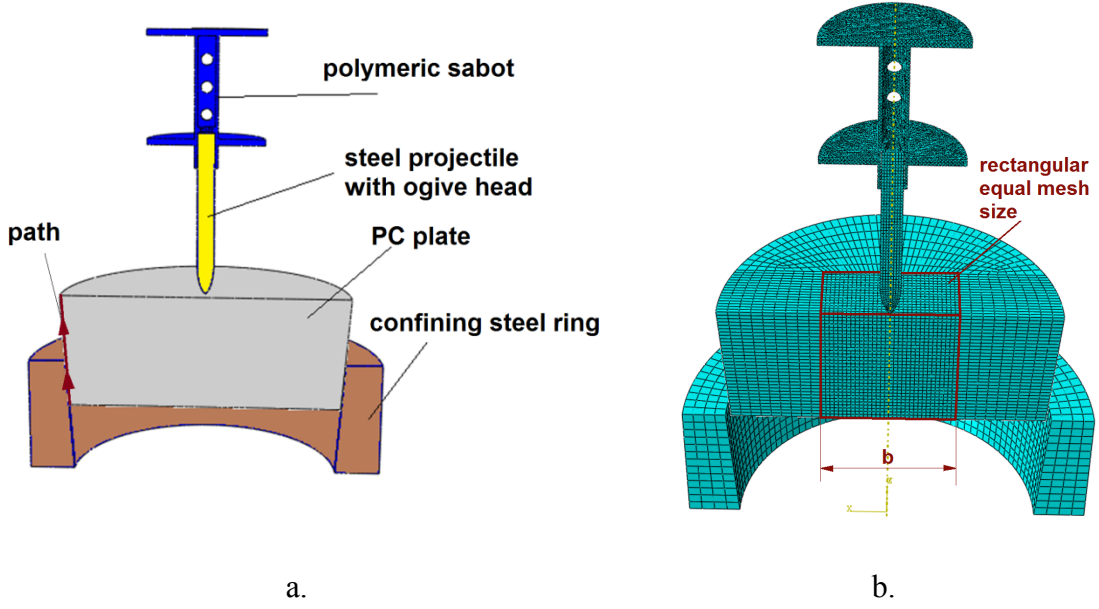
a.

b.

Figure B2: a. The assembled confined model at the beginning of the numerical analysis. b. The meshed assembled confined model showing the region of equal mesh size on the PC plate.

The entire assembly contain a total number of 51409 nodes and 65741 elements: 39922 linear hexahedral elements of type C3D8R and 25819 lineat tetrahedral elements of type C3D4. A rectangular box cell of the PC target, shown in Fig. B2b and having the size $b \times \dfrac{b}{2} \times H$ where b=H=40 [mm], was meshed with equal size hexahedral elements of type C3D8R. The region adjacent to the projectile trajectory must be meshed with equal mesh size because the numerical results are mesh dependent ([16]).

B.3 Analysis

   A 3D transient adiabatic analysis was conducted with the commercial FE code Abaqus/CAE [19]. The hydrodynamic continuum equations are derived from application of the conservation laws of mass, momentum, and energy. An equation of state provides the relationship between pressure, density, and internal energy. An elastic-plastic Mises plasticity model is used for constitutive relations. An overview of the theory of hydrocodes can be

33

found in [26]. The constitutive behavior of polycarbonate was represented using a hydrodynamic material model in which the material's volumetric strength is determined by a linear Mie–Grüneisen equations of state [27] while the deviatoric behavior is of the isotropic elastic-plastic Mises-type. Two failure criteria [27]: (1) tensile failure (2) ductile damage with damage evolution, were used. These failure criteria will be detailed in Section 3.4.

The general contact algorithm of Abaqus [19] was used with element-based surfaces which can adapt to the exposed surfaces of the current non-failed elements. All the surfaces that may become exposed during the analysis, including faces that are originally in the interior of body were included in the contact model. This means that we included all the elements of the plate, projectile and sabot in the contact domain since the projectile trajectory is not known a priori. We chose the software parameters so that contact nodes still take part in the contact calculations even after all of the surrounding elements have failed. These nodes act as free-floating point masses that can experience contact with the active contact faces. A frictionless contact was assumed to exist.

The simulations of the confined targets were performed in two steps:

1) Insertion and confinement.

2) Impact.

The simulation of the unconfined target was performed with only one step : 1) Impact. The insertion step is comparably long to avoid inertia effects and to mimic a quasi-static insertion. It lasts for 1000 [μs]. It was verified that the effect of the kinetic energy during the insertion is negligible. At the beginning of the impact step it is negligible in comparison to the total internal energy. It was also verified that the confining stress distribution is similar to the distribution which is calculated quasi-statically using axisymmetric mesh. Fig. B.3 shows the distribution of the radial confining stress along the path shown in Fig. B2a. The distance from the bottom of the PC plate is normalized by the deformed length of the path. The difference is less than 10% and is due to the different material models which were used in the analyses.
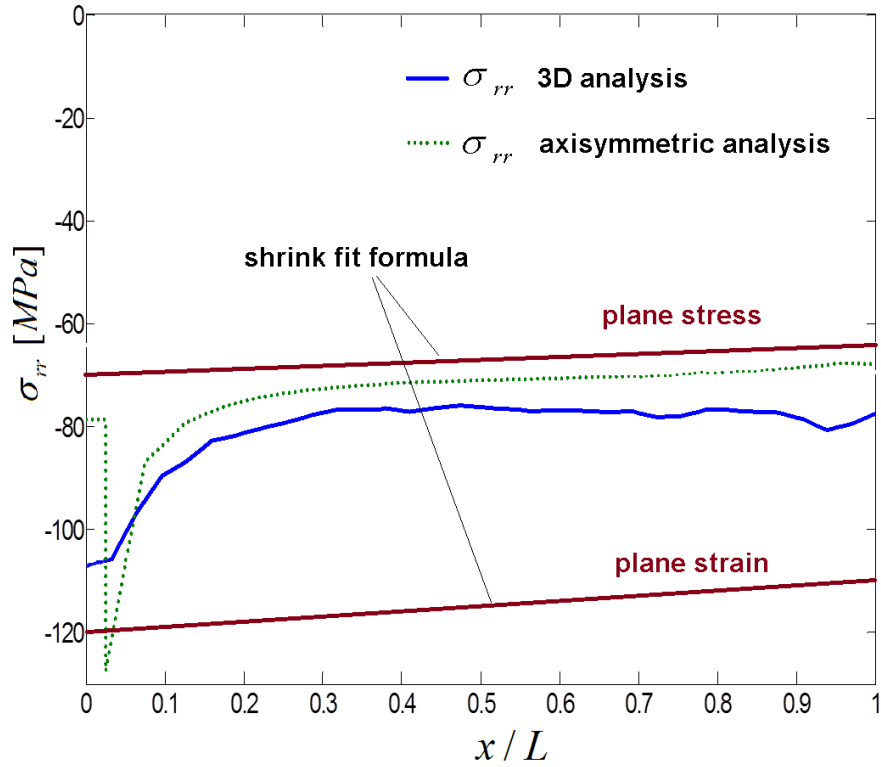
Figure B3: Comparison of the confining radial stress along the normalized path length x/L (L is the length of the path, x is a coordinate along the path) shown in Fig. B2a which was obtained numerically in the end of the insertion step using 3D explicit analysis with Mie-Gruneisen equation of state for the PC and static axisymmetric analysis using elastic-plastic Mises plasticity   for the PC. The average difference is less than 10%. The prediction of the elastic shrink-fit formula for cylindrical bodies is show as well [http://www.amesweb.info/InterferenceFit/InterferenceFitCalculationSteps.aspx#.U_Hz6P mSyE0].

The (next) impact step lasts for 600 [μs]. During the insertion step displacement are applied on the upper face of the PC plate while the bottom face of the confining ring is held fixed by application of symmetry conditions. Frictionless contact is assumed between all contacting surfaces during the impact step. A coefficient of friction 0.2 was assumed during the insertion step between the contacting faces of the PC target and the confining steel ring to avoid jump up of the PC plate in the end of the insertion step. During most of the insertion step the sabot and projectile are held fixed. Close to the end of this step, the sabot and projectile are accelerated to the desired velocity. At the end of the step the tip of

the projectile almost touches the inserted PC plate. During the impact step, the displacement on the upper face of the plate, as well as the symmetry conditions on the bottom face of the confining steel ring, are released. Only the impact of the sabot and projectile having initial velocity, which was obtained in the previous step, act upon the confined target.

B.4 Material models and failure parameters

B.4.1 Sabot

The sabot weighted 6.5 [gr] and was solid-printed from FullCure720, which is a rigid general purpose semi translucent acrylic-based photopolymer. An elastic plastic material model was used with Mises plasticity. For this material, the density used is ρ=1050 [Kg/m^3] and Young's modulus E = 2.87 [GPa] with Poisson's ratio υ = 0.35. The yield stress is σ_y = 60 [MPa]. A small linear hardening was assumed with E_p = 5 [MPa]. The ductile failure criterion of [19] with no damage evolution. The equivalent plastic failure strain was 0.2 for all strain rates and triaxialities.

B.4.2 Projectiles

The projectiles were made of hardened 15-5 PH stainless steel with density ρ=7800 [Kg/m^3] and weighted 11.4 [gr]. An elastic-plastic material model was used with Young modulus E = 210 [GPa] and Poisson's ratio υ = 0.3. Mises plasticity was assumed with a yield stress σ_y = 1.5 [GPa], and (linear) hardening modulus of E_p = 1.67 [GPa]. No failure criterion was used since the hard steel projectile did not fail.

B.4.3 PC plate

A hydro-dynamic material model in which the material's volumetric

strength is determined by an equation of state was used for the polycarbonate plate, namely the Mie–Gruneisen equation of state (EOS) with application of linear U_S-U_p Hugoniot. U_S is the linear shock wave and U_p is the particle speed. This model can be applied to materials which also have isotropic elastic or viscous deviatoric behavior. It is used with a Mises plasticity model. More details can be found in Abaqus Analysis User's Manual in chapter: 21.2.1 equation of state [27]. The hydrodynamic material data for the polycarbonate was taken from [28] who used the AUTODYN material libraries. The isotropic elastic linear shear behavior was given a value of 803 [MPa] at room temperature and a value of 80.3 [MPa] for temperature elevation of 200° [C], based on [29]. The PC material parameters are summarized in table 1. The strain rate and temperature dependence of the plastic behavior is shown in Fig. B.4. The strain rate dependence is based on our experimental results with cylindrical specimens [30], and uses a linear extrapolation for large plastic strains. The strain stress curve for strain rates exceeding 8000 1/s was assumed to be identical to that of 8000 1/s. This extrapolation is used due to the lack of experimental data. It was assumed that at $\Delta T = 100^o$ [C] for all strain rates, the PC softens and the yield stress is half of the quasi static one, while at $\Delta T = 200^o$ [C] it drops almost to zero, and the material flows freely [29].
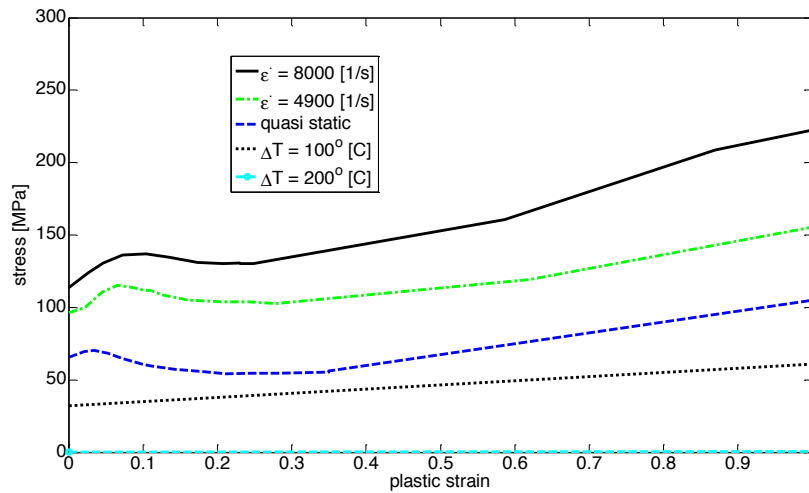

Figure B4: Flow properties of polycarbonate which were used in the

numerical analyses.

Table B1: Material parameters used in the analyses for polycarbonate.

	Density ρ [Kg/m^3]	1200
Elastic and Physical properties	Young's modulus E [GPa]	2.2
	Poison ratio v	0.370
	Specific Heat C$_p$	1300
	Inelastic Heat Fraction	1
Hydrodynamic data (Hazell *et al.*, 2008)	Reference density [kg/m^3]	1910
	Bulk sound speed [m/s]	1933
	Slope s in Us versus Up diagram	2.65
	Gruneisen coefficient	0.61

Two failure criteria [19,27]) which were used and fully derailed in [16] were used *simultaneously* : (1) Ductile failure with damage evolution. (2) tensile failure. An element was deleted from the analysis when one of these two criteria was first fulfilled. The plastic failure strains for different strain rates and triaxiality (t_r) are detailed in Fig. 5. The negative triaxiality (pressure) causes a rise in the failure strain. This is the only difference in the material properties which are used here in comparison to what was used in [16]. These values were calibrated by fitting the velocities of the projectiles and their depths of penetration to the experimental results. The damage evolution was modeled by an equivalent plastic displacement at the point of failure : u_p^f = 80 [μm]. In the second criterion the "tensile failure" value was set to 160 [MPa] .